Pressure deficit in Gale Crater and a larger Northern polar cap after the MY34 Global Dust Storm.

Manuel de la Torre Juárez[1], Sylvain Piqueux[1], David M. Kass[1], Claire E. Newman[2], Scott D. Guzewich[3]

[1]Jet Propulsion Laboratory/California Institute of Technology, Pasadena, CA, USA
[2]Aeolis Research, Pasadena, CA, USA
[3]NASA Goddard Space Flight Center, Greenbelt, MD, USA

Key Points:

- A technique to measure representative pressure scale heights at Gale enables tracking of signatures of changes in the polar ice caps.
- REMS surface pressure with Mars Climate Sounder observations are used to describe the polar processes after the great storm of Mars Year 34.
- Multiannual pressure data show a short Southern Polar Cap growth season before the storm followed by a long Northern Polar Cap growth season.

Plain Language Summary: In 2018, Mars Year 34, Mars experienced a dust storm that encircled the whole planet and darkened its skies more than most storms in the recent past. Already in 2019 an analysis of the effects observed after the storm reported surface pressures below the climatological values observed over the previous 3 years in Gale Crater. The pressure deficit persisted into Mars Year 35 long after the end of the storm and dust over Gale had returned to levels from previous years. The storm coincided with a longer duration of the condensation season of the North Polar ice cap and a subsequent increase in its maximum amount of ice volume. We perform here a full analysis of five Mars Years of data showing how the duration of the polar caps sublimation/condensation seasons changed around the time of the storm, that the extension of the polar caps changed, and that the atmosphere above the North Pole was slightly colder than in years before the storm.

Corresponding author: Manuel de la Torre Juárez, `mtj@jpl.caltech.edu`

Abstract

We describe the model-independent analysis technique of Mars Science Laboratory (MSL) pressure and Mars Climate Sounder (MCS) data in de la Torre Juárez et al. (2019) that compared multiple years of surface pressures on Gale before, during, and after the Global Dust Storm of Mars Year 34. The analysis found (1) representative pressure scale heights over Gale; (2) that the storm was followed by a pressure deficit at Gale; (3) the following C storms did not eliminate the deficit; (4) changes in the duration of the polar caps condensation seasons, with an early start of the North Polar (NP) ice cap growing season the year before the Great Dust Storm (GDS) and a late signature of the end of the expansion season thereafter, changes consistent with a larger growth phase of the NP cap; (6) MCS observed a larger than usual NP cap; and (7) cold temperature anomalies over the NP and warm over the Southern Pole after the storm.

We also show that the analysis of observed MSL pressure data alone filters out effects on the pressure signal that are attributable to dynamical and orographic processes in a recent model analysis that makes similar interpretations as our 2019 study. One additional Mars year of observations is included to eliminate early concerns about sensor drifts. Noting that a similar NP anomaly was observed with MCS data after the last early GDS in MY25, and not the later GDS of MY27, the results suggest a possible unique effect of early GDSs.

1 Introduction

The recent Global Dust Storm (GDS) of Mars Year 34 (MY34) is not the first one whose effects have been measured from the surface of Mars. Decades ago, instruments aboard the Viking Landers captured the influence of three planet-encircling dust storms on the near surface micrometeorology at two different locations (e.g. Ryan & Henry, 1979; Tillman, 1988, and references therein). The recent GDS witnessed by Curiosity and the different times and locations between Curiosity and the Viking Landers help characterize the range of surface phenomena associated with dust storms. Curiosity covered longer time periods before and after the GDS than those that Viking could sample. The comparison of both data sets helps verify the predictions from different models (e.g. Hourdin et al., 1995; Newman et al., 2002; Medvedev et al., 2011; Zhao et al., 2021, and references therein). Some model predictions can agree while others sometimes contradict observations (e.g. references in Piqueux et al., 2015, for a brief summary). The recent MY34 GDS experienced by Curiosity provides also an opportunity to discern what effects of dust storms on the martian atmosphere are robust over time and if dust storms can affect and therefore leave a signature in the seasonal stratigraphic record of our neighboring planet's polar caps.

Compared to previous planet encircling storms (see the surveys in e.g. Zurek & Martin, 1993; Wang & Richardson, 2015), the MY34 GDS had an early onset at areocentric longitude $L_s \sim 190^o$ and reached higher dust opacities than those of the Viking Lander era, while likely less than others that could not be measured from the surface such as the 1971 Mariner observed GDS (e.g. Zurek & Martin, 1993). The environmental response near Gale's surface was monitored by Curiosity's Rover Environmental Monitoring Station (REMS) from 4.5°S latitude, a near-equatorial location compared to the northern latitudes of the Viking Landers 1 and 2 at $\sim$ 22.3°N and 47.6°N. During the Viking era, the three planet encircling storms were reported at $L_s \sim 204°$ and 268° in 1977, and $L_s \sim 208°$ in 1982 (e.g. Ryan & Henry, 1979; Zurek & Martin, 1993). Curiosity first experienced the MY34 storm at $L_s \sim 190° - 195°$ (in Guzewich et al., 2018; Viúdez-Moreiras et al., 2019), an onset time only preceded recently by the $L_s \sim 180°$ MY25 storm (e.g. Wang & Richardson, 2015) whose effects were not observed from the surface. Viking registered changes to the local temperatures, atmospheric opacity, and winds as well as to the pressure tide signatures of the large-scale planetary scale circulation caused by dust storms (Ryan & Henry, 1979; Tillman, 1988; Wang & Richardson, 2015). Effects at both types of spatial scales have been reported for Curiosity as well during the MY34 GDS (Guzewich et al., 2018; Viúdez-Moreiras et al., 2019) with several features shared by Viking reports that include changes in pressure tide amplitudes and phases. REMS observed other responses that have been proposed by models, such as changes in the time of the day when the transition from a stable to unstable boundary layer occurs, when do topographic flows develop, the strength of convective activity, or the stability of the boundary layer measured by a change of sign of near surface lapse rates (Viúdez-Moreiras et al., 2019) all of which could not be verified by Viking. Some model analyses (Wood & Paige, 1992; Hourdin et al., 1995; Newman et al., 2002) explain that local observations (in Ryan & Henry, 1979) can be related to shifts in the Hadley Cell (Hourdin et al., 1995), suppression of atmospheric waves (Tillman, 1988), and changes in surface albedo and emissivity at the poles that might modulate the polar CO_2 condensation-sublimation cycles. However, to our knowledge, few studies had a long enough observational data record to compare the multi-annual background climatology and, therewith, the effects of dust storms from several Mars years before to the full year after the storm had passed.

Today's orbital assets, in the form of the Mars Climate Sounder (MCS), the MARs Color Imager (MARCI) on the Mars Reconnaissance Orbiter (MRO), plus the surface cameras (Bell et al., 2017) and the environmental REMS sensors (Gómez-Elvira et al., 2012) on the Mars Science Laboratory (MSL) rover, have gathered a multiyear record of atmospheric measurements of the Martian atmosphere. Additional sensors on the InSight lander, which measured more than one year of nearly continous pressure, temperature, and wind data after the GDS, or the Perseverance rover, which carries the Mars Environmental Dynamics Analyzer, MEDA, provide far denser sampling of atmospheric phenomena from the Martian surface than what was possible during the Viking era.

In this manuscript we describe and extend the observation-based results and approach used in de la Torre Juárez et al. (2019) with a larger dataset. It found that shifts in the phasing of the CO_2 condensation-sublimation cycle can leave a measurable signature long after a global dust storm ends. This work also includes one additional Mars year of data to address the following concerns about the initial study. First, the risk of potential sensor hardware drifts with time. Second, the correct estimation of the influence of changes in rover height on pressure data through a constant pressure scale height when a year was included where pressure had been strongly perturbed by the GDS. This dust influence on Gale could raise apparent non-existent deficits in pressure (Lange et al., 2022). Third, eliminating the influence on REMS pressure data trends from regional dust storms that followed the GDS. For instance, the C storms occurring typically during $L_s = 300° - 355°$), leave a signature in orbital MCS data (Kass et al., 2016),and in surface pressure data (e.g. Zurita-Zurita et al., 2022). Last, about the influence of other dynamical phenomena caused by the planetary orographic difference between Northern and Southern hemisphere as well as geostrophic adjustement effects (e.g. Hourdin et al., 1993; Hourdin et al., 1995). Section 2 discusses: (1) model-independent fits to observed daily average pressures to determine representative pressure scale heights for Gale; (2) how the $\sim 2.5 - 5$ Pa pressure deficit detected in de la Torre Juárez et al. (2019) that was perturbed by dust preceding the C storms season, reappeared and survived long after the opacity caused by the GDS and the C storms had returned to typical levels. The orographic and dynamical concerns are dispelled in recent arguments (Lange et al., 2022, section 3.2) that use a different analysis that combines model output, REMS, and InSight data to support the original interpretation of the pressure deficit over Gale as related to changes in the polar cap. The extension here of the REMS analysis by one Mars year confirms that also the observation-based approach of the original work is free from such concerns. Further, section 2 describes and compares over several years the duration of the sublimation-condensation cycles of the polar caps through their signature in the timing of pressure minima and maxima. It describes where the extra year of data unveils the unique character of the year before and the year after the MY34 GDS. The extra year of pressure records is also useful to confirm that the observational analysis compensated for sensor trends that might exist. The logical argument in the original REMS observational analysis then used that surface pressure is to first order a measure of the weight of the atmosphere, that the strongest contribution to this signal in the annual cycle is driven by the polar sublimation and condensation of CO_2 at the polar caps, and that model predictions show a shift in the timing of the annual cycle at the Poles with changing opacity (e.g. Hourdin et al., 1995; Kahre & Haberle, 2010) caused by the combined effects of warmer atmosphere and altered emissivity and albedos at the polar caps (Wood & Paige, 1992). Section 3 describes how we explored with MCS data the hypothesis about changes in the polar caps that was formulated to explain the pressure deficit: if this pressure deficit was a signature of changes at the polar caps following the northern hemisphere (NH) fall of MY34.

Section 4 describes the MCS data analyses also in de la Torre Juárez et al. (2019) of the atmospheric column above both Polar caps to provide modelers with observations that might validate or constraint their results. As an example, recent model sensitivity analyses (Zhao et al., 2021) have shown that dust storms may affect the polar cap cycles. The last section summarizes and analyzes the results.

2 Data, Approach and Results from REMS Pressure Data:

A combination of data from REMS (Gómez-Elvira et al., 2012) are used here to establish the seasonal pressure cycle expected on Gale from the data collected over all years MY31-MY36 since Curiosity's landing. This pressure cycle is then compared in the next section to MY34 measurements by MCS (McCleese et al., 2007) aboard the Mars Reconnaissance Orbiter (MRO) (Zurek & Smrekar, 2007) during and after the GDS. The size of the seasonal polar cap is determined from MCS observations for MY 34 and comparisons among previous years following the storm (Piqueux et al., 2015). The timeline used to describe the cadence of events follows that described in Guzewich et al. (2018); Viúdez-Moreiras et al. (2019) which are based on a combination of MCS, Curiosity's Mast Camera (MCAM) (Bell et al., 2017), and REMS observations.

2.1 REMS Pressure data, climatology, seasonal and altitude effects:

A pressure climatology of REMS sol averaged pressure data was developed with an effort to identify seasonal and altitude effects. The sol averaged surface pressure was obtained from the REMS pressure sensor baseline sampling rate that consists of the first 5 minutes after the start of each Local Mean Solar Time (LMST) hour. REMS regularly adds extended sessions at least 1-hour long to capture the details of events and oscillations that last under one hour. The extended sessions shift their starting time from one Martian day, or sol, to another. A fit (equation 1) to the observed surface pressure during the first 5-min of each hour was made to a series of 12 subharmonics of a sol period after expressing time in terms of hour fraction of Local True Solar Time (LTST), since LTST reflects more accurately the solar orientation over the sol cycle. The fit parameters were the sol pressure mean $\bar{p}_s$, the tidal p_n amplitudes, and their phase shifts, t_n. The REMS pressure record started on sol 10 after landing and has run observations daily since then with a few missing sols due to limitations imposed by planetary conjunction, rover software updates, or short periods of rover anomalies. For this analysis only sols with at least 23 5-minute sampling blocks were used to calculate the diurnal pressure averages.

$$p(t) = \bar{p}_s + \sum_{n=1}^{12} p_n \sin\left[2\pi\left(n\frac{LTST}{24} - t_n\right)\right] \quad (1)$$

After obtaining the sol average pressures, $\bar{p}_s$, from all these years, they were fitted through least squares minimization to a second series of harmonics of areocentric longitude L_s, measuring the angle Mars has covered in its trajectory around the Sun after passing the Northern Spring equinox as the independent variable to track time, modulated by an exponential correction that represents the thinning of the atmosphere with height, z, as the rover has been traveling up the crater (the modeling and observations of the thinning of the atmosphere with height can be traced back at least to Pascal, 1648). Withers (2012); Tyler and Barnes (2013); Richardson and Newman (2018) give a complete discussion specific to Gale:

$$\bar{p}_s(z, L_s) = \left[p_{s0}(z_0) + \sum_{n=1}^{12} p_{sn} \sin\left(2\pi\frac{nL_s - L_{sn}}{360^\circ}\right)\right] e^{\left(\frac{z_0 - z}{H}\right)} + \Delta \quad (2)$$

H is a free fit parameter that represents the rate at which pressure decays with height and is not prescribed. L_{sn}, p_{sn} and p_{s0} are additional fit parameters that capture the seasonal variability of the pressure cycle Δ is the difference between the observation and the fit. In an isothermal atmospheric layer H is the pressure scale height and therewith related to the temperature, $T(z_0)$, of that layer through H$=-g/RT(z_0)$, with $g = 3.71$ ms^{-2}, gravity, $R = 8314/43.3$ m^{2}K^{-1}s^{-2} the gas constant for the Martian atmosphere, and z_0 a reference height for that layer. Because the atmosphere is not isothermal, using temperatures from a model to infer H includes many uncertainties. These include what should be the height that $T(z_0)$ really represents. Since the boundary layer can have steep gradients, the REMS near surface air temperature cannot be used. There is also the related question of what is the appropriate atmosphere thickness to relate that modeled H, to the data. The approach was to look for a temporal window where the rover had travelled a large enough height interval, Δz, to be able to notice the height dependence. The bigger the time interval, the bigger the height covered and the better the accuracy of the pressure scale height. As the rover accumulated a large Δz, the seasons also evolved and left a mark. Pressure data fitted to equation (2) over 1 Mars year was found to be enough, but taking multiple years for the fit allows to identify a height dependence less subject to interannual variability or to anomalous dust years. However, thinking on relating H to a model, since temperature and dust opacity change with time of the day or season, it is not clear how does one infer a fixed H from the models to match the REMS data collected over multiple years. These issues do not affect the pressure data-only analysis described here. The only use intended for H and $T(z_0)$ values was for an order-of magnitude comparison with previous authors (e.g. Withers, 2012; Richardson & Newman, 2018). The fit to equation (2) was then used to detect the time occurrence of deviations from the observation, Δ, where phenomena occur that are not captured by the seasonal pressure cycle and the exponential thinning of the atmosphere with height.

To understand if the effect of the seasonal dependence of H in the fitted results is robust, different temporal windows of REMS data are shown here, which results in different values of H. The comparison of results for different time windows shows what deviations remain for multiple values of H. Multiple fits are done to different parts of the full traverse using the first three, four, five years and an intermediate time on sol 2440, contemporary to the analysis in de la Torre Juárez et al. (2019), to compare major changes in the shape of Δ. In each part of the traverse the reference height, z_0, was fixed to the center height of the range of altitudes covered in that time window.

For a five-year fit the height $z_0 = -4239$ m is the reference altitude for the resulting fitted pressure. A different test is found in de la Torre Juárez et al. (2019), where H was estimated from the data as a function of L_s. It adds validation to our conclusions by comparing what pressure biases are common with the fits to a constant H. Note that the fit to obtain $H(L_s)$ only had four years for each value of L_s and is therefore sensitive to the possibility one of those years being an outlier during the GDS.

2.1.1 Sensor drifts and differences, Δ, between observations and fit:

Differences between the data and the fit have two causes, either instrumental errors, or natural phenomena, such as those that do not follow the seasonal cycle and the thinning of the atmosphere captured in equation (2). The REMS measures pressure using 6 barometers with different response times and long-term stability characteristics. These barometers are grouped into two independent oscillators, or pressure sensors, that were required before launch to have an error below 1 Pa per sample (Gómez-Elvira et al., 2012). REMS undergoes regular recalibrations since landing to detect and minimize any long term trends caused by the sensors. This correction ensures that long term drifts remain at or below the values of 0.5 Pa per year predicted in Harri et al. (2014). Intercomparisons of the two most stable REMS oscillators show a drift smaller than 0.5 Pa between them, but lacking an independent calibrated cross-reference barometer on Mars, it is impossible to separate the actual slow sensor drifts from drifts in pressure values due to natural causes. However, the exponential dependence in the fits to equation (2) would correct at least partially for linear sensor trends because the Taylor expansion of an exponential function of height starts with a constant plus a linear function of height. When a linear fit $\Delta = c_0 + c_1 \cdot Sols/N$, where N is the total number of sols for the fitting window, is made to the difference between the observation and the fit to equation (2) to the data of 3, 4, and 5 full martian years since landing, the total linear trend of the resulting Δ was: c_1=0.077 Pa/3 years, c_1 =0.015 Pa/4 years, c_1 =0.341 Pa/5 years. This means that a combined long-term contribution to Δ from trends in the sensors and natural variability is a fraction of 1 Pa for the full 5 years. This is, less than half a Pascal is an upper bound for the contribution from sensor trends to the fit anomalies $|\Delta|$.

2.2 Fit results and Differences between fit and observations:

Figure 1 shows the dust opacity in the upper third subpanel measured over Gale by MCAM. The fit to the harmonic series is shown in the bottom panel as a dashed blue line overlaid on the red line that represents the averages obtained with equation (1). The dust opacity shows the timing of the different dust seasons and allows a comparison between the magnitude of smaller, regional dust storms (which occur every year) and the GDS. The central section shows the difference, Δ, between the blue line representing the fit and the observed values, extending this analysis from the 2440 sols (∼3.6 Mars years) shown in the Figure 1(b) upper panels when the deficit was first detected to now cover the first 5 Mars years of the mission. Subtracting the fit removes essentially the contribution of the altitude changes and seasons. REMS first 5 Mars years since landing, until sol 3353, were used to find a constant scale height, H, that produced the smallest standard deviation between the fit and observations. The result is shown in Figure 1(a) central panel, which gives a standard deviation between fit and observation of 2.4 Pa. The seasonal dependence of H is absorbed into the series of sine functions. A possible deviation between the observations and an exact subharmonic of the year may be responsible for the spurious short lived peaks near sols 1690 or 2040 that could reflect a shift in the phase not captured by the subharmonics of one year. This happens for instance when there are delays in the CO_2 sublimation-condensation cycle at the Poles that could shift one pressure minimum but not the other.

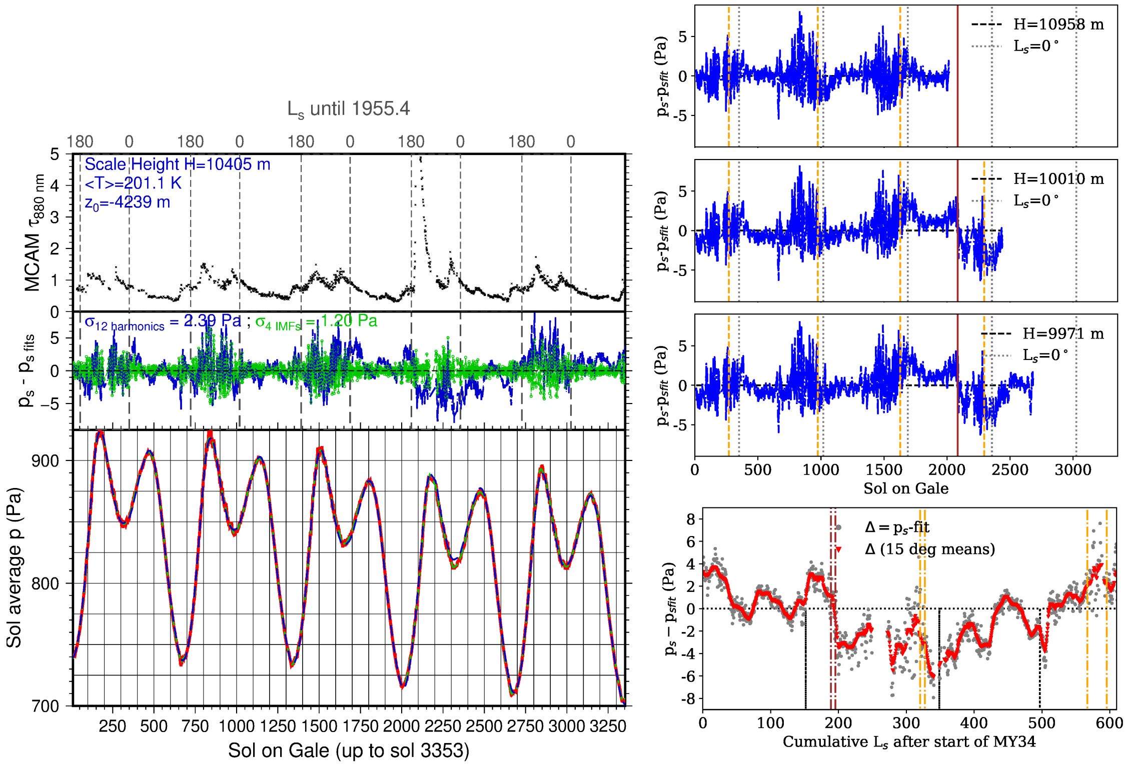

(a) (b)

Figure 1. (a) Bottom panel shows the pressure as a function of season and height. Red shows the observed annual means obtained from eq. 1 and the blue dashed line the fit to (2). A green dashed line marks the sum of the first 4 empirical functions from a Hilbert Huang transform with a sifting condition chosen to minimize the standard deviation between the 4 modes and the observed pressure averages. The center plot shows in blue the difference, Δ, between observation and fit to equation (2) and in green against the Hilbert-Huang empirical filter. Δ includes the exponential height dependence of pressure. The top panel shows the opacity changes obtained from the MCAM instrument 880 nm filter. The green anomalies in the center plot show no trend and its difference to the blue anomalies marks times where the sol averaged surface pressure differed from a seasonal behaviour that is consistent with a series of subharmonics of the annual cycle. Column (b) Shows three upper panels with fits to (top) 3 Mars years in Gale, before the start of the storm, Sol 2440 (middle), before end of the MY35 but covering the global dust storm period, and (bottom) four full Mars years in Gale. Each fit used a different reference altitude z_0. Vertical dashed orange lines mark the sol with peak MCAM opacity associated with the C storms and brown for the peak opacity of the GDS. The bottom panel of this column shows in detail pressure anomalies from MY34 and early MY35 starting from $L_s = 0$ of MY34 and ending on $L_s = 154$ of MY35 after another big dust storm covered Mars. Open circles show the anomalies, To guide the eye red symbols track a running average of Δ with a window of 15° in L_s.The dotted line marks the zero reference and the moments where the pressure reached its annual minima in MY34 and beginning of MY35. Those mark the approximate moment of maximum extent of the Northern Polar (NP) and Southern Polar (SP) ice caps at the MY34-SP $L_s = 151.45°$, MY34-NP $L_s = 343°$, and MY35-SP $L_s = 496°$. Vertical brown lines mark the growth phase of the GDS, orange lines mark the full growth phases of the following C and Z storms periods.

For signals with such phase shifts, other filtering techniques like maximum entropy (Tillman, 1988) or Hilbert-Huang (HH) empirical mode analysis have been shown to eliminate those spurious signals in the harmonic analysis (e.g. Huang & Wu, 2008). HH has the ability to separate efficiently between nonlinear trends associated to different time scales in observed signals. It was therefore chosen to compare with the fits to equation (2) and cross-validate the contribution of the observed weather variability. This enables comparisons to theoretical predictions from Lange et al. (2022) that used model sensitivity analyses to estimate by how much errors in temperature estimates could lead to a non-representative H in equation (2). This could happen in our case when one choses an inadequate time window, with its associated Δz. It would lead to an incorrect scale height that does not capture the overall variability of temperature, and therefore H, as weather changes at the MSL location. So, in addition to the spurious higher harmonic errors, if the fits to equation (2) don't find a representative H, misrepresenting the influence of the weather would add to apparent subseasonal variability in the harmonic fit from imposing a constant H. But if the fitted H is a good representation, this difference should have comparable magnitudes between both, HH, which is free from the spurious harmonic mode errors, and the fits to equation (2).

HH analysis empirically separates a complex time signal into modes, Intrinsic Mode Functions, IMFs, that have decreasing numbers of crossings through the signal's mean value and, therewith, decreasing numbers of maxima and minima. The first IMF is obtained by creating two envelopes, an "upper" envelope that connects via cubic spline interpolation all the maxima in the pressure data record, and a "lower" envelope that connects all the minima. To complete each envelope, the interpolation from the first/last maximum/minimum to the end of the data interval is a cubic spline connecting that first/last maximum and minimum with its mirror reflection on the other side of the closest end of the data interval. The average of both envelopes, a "protomode", is calculated at each data point. Then the protomode is subtracted from the full signal and new upper and lower envelopes are created for the difference between observation and protomode. This process is iterated, "sifting", until the difference between a protomode and the one from the previous iteration is negligible. The residual between observation and converged protomode is the first IMF. It typically has the highest number of maxima and minima of all the IMFs. To find the second IMF, the first is subtracted from the observed data and the same sifting process is now performed on this difference. The decomposition continues until the last IMF has only one crossing through the mean value of the signal, typically resulting in one maximum and one single minimum in the full interval.

The HH decomposition is not unique but its ability to separate time scales and the effect of weather systems and planetary waves on pressure at Gale has been discussed and used elsewhere (Haberle et al., 2018; Zurita-Zurita et al., 2022). To compensate for the non-uniqueness and the fact that there is some arbitrariness in the choice of the convergence criterion, we use between 6 and 16 sifting iterations, but select the one that minimizes the standard deviation of the differences between the last 4 IMFs and the observation. In Figure 1(a) center panel the difference between the observation and a HH filter with the sum of the slowest 4 empirical modes is also shown as green dashed lines in the central panel. It shows that the standard deviation between the temperature independent HH filter and the observed average daily pressure is 1.2 Pa. This result suggests that the effect of 3σ outliers attributable to weather in our filtering -either with HH, $3\sigma \sim 3.6$ Pa, or to errors from fixed H, $3\sigma = 3 \times 2.4 \sim 7.2$ Pa- are lower than the prediction of 15 Pa-20 Pa when selecting the wrong H for Gale at this location (Lange et al., 2022) and lower than the main anomalies discussed later. This 3σ value is comparable to the value obtained in the full analysis that includes the Mars Climate Database model (Lange et al., 2022), where their interpolation method results in a similar 3σ to our method.

The bottom panel of Figure 1(a) shows the sol pressure averages obtained for sols 10 to 3353 since the landing of the Mars Science Laboratory spanning from Mars Year 31.43 to 36.43. The figure only shows the first full five years or cumulative L_s=155° to cumulative $L_s = 1955.4°$, where the cumulative L_s is obtained by not resetting the areocentric latitude each time L_s crosses 360°. To enable quantitative comparisons with previous works (Tillman et al., 1993; Hourdin et al., 1995), the fit (2) to the annual cycle is done in this figure with a series of 8 harmonics, when mentioning later in this work the numerical amplitudes of the fundamental harmonic, and with 12 harmonics for the figures because 12 modes is equivalent to a ∼57 sol low-pass filter. The differences, Δ, between the observed pressure and their fits, are magnified in the central panel of Figure 1(a) as a blue line for the exponential fit with altitude dependence and green for the difference between the observation and the slowest 4 empirical modes of a Hilbert-Huang filter. This empirical filter is used to validate the oscillations associated with different temporal scales versus changes caused by the interannual differences from when the maximum or minimum pressure are obtained, since harmonic series would not capture those shifts and lead to an artificial error. Observations remain within ∼ 5 Pa of both approaches.

The higher frequency variability associated with waves shows two distinct patterns, depending on whether the REMS observations were made during the dusty or the clear seasons of the Martian year. For the first 50 sols of the mission and during sols 400–650 there is an apparent oscillation with circa 3 peaks and a time separation of ∼ 17 sols that has been associated with baroclinic wave activity in Viking landers (Ryan & Henry, 1979; Barnes, 1981) and REMS data (Haberle et al., 2018; Zurita-Zurita et al., 2022). On a slower temporal scale, an offset is visible after the MY33 dust storm season that was not addressed in Haberle et al. (2018). This slowly evolving anomaly, displayed as a rapidly growing positive pressure bias in the blue lines starting near sol 1700, reached its peak of ∼3 Pa and slowly returned to zero. It was then followed by a second bias period that started slowly near sol 1960, grew to a peak and then recovered rapidly, overshooting and changing sign into a low surface pressure bias. The top panel of Figure 1(a) shows the MCAM opacities for the full record, and that the overshoot occurred during the MY34 global dust storm.

To see if the deficits in MY33 and MY34 were an effect of using a constant H that ignores the seasonal dependence of H, an effect of fitting to low dust years, or an effect of other dust storms after the GDS, the three upper panels of Figure 1(b) show three different lengths of pressure records and vertical lines marking the peak opacity of the C storms in orange and the GDS in brown. Starting at the top, the three panels show a time window of all sols up to 10 sols before the start of the GDS (top), 2440 sols -a few sols earlier than those used in de la Torre Juárez et al. (2019)-, and (third panel) four complete years since landing. The bottom panel in Figure 1(b) shows more detail about the time where the pressure bias lasted and marks the full growth time of the GDS, and the subsequent C and Z storms, $L_s \sim 120° - 160°$, (e.g. Zurita-Zurita et al., 2022).

Figure 1(b) upper panel with only the low dust years, data until 10 sols before the beginning of the GDS, removes the two bias peaks in MY33 seen in Figure 1(a) central panel. Closer visual inspection, and including the high dust year (MY34) shows an unusual change of H. This suggests that the positive pressure bias of MY33 seen in Figure 1(a) or the two others in Figure 1(b) emerges when the fit includes the high dust scenario of MY34 and overcompensates by introducing a linear trend to the previous years in all the fits that included the period of the GDS. This effect causes an apparent positive trend and bias in MY33 that is absent in the top panel of Figure 1(b). Additionally, this analysis shows that in every year the C storms are preceded by a positive pressure anomaly that the storms then eliminate without introducing any biases. This is opposite in sign to the immediate response and thereafter long-lasting negative anomaly observed after the GDS.

Figure 1(b) bottom panel shows that the GDS occurred during a decreasing pressure trend and the storm did not change this trend. Then, a positive pressure anomaly occurred before the start of the MY34 C storms season, near $L_s \sim 320°$ nearly eliminating the deficit, but then the growth of the C storms returned the pressure deficit to the pre-existing biased values. It was only when the NP cap started retreating, near $L_s = 343°$, that the pressure deficit started disappearing and Δ continued increasing until after the L_s where the SP cap had reached its maximum extent.

The slow positive and then negative differences of MY33 and early MY34 between fit and observation are consistent with a heavier atmosphere after the dust storms season of MY33 and with the dust storms season of MY34 leaving behind a lighter atmosphere. These slowly evolving pressure biases still overlapped with the rapid oscillations, typical signatures of baroclinic-type and other waves, indicating that the cause of the slow pressure biases evolved on a different time scale and was therefore a manifestation of a phenomenon other than the more rapid fluctuations associated with weather and baroclinic activity.

2.3 Timing of the pressure markers of the Polar Ice Cap cycle:

To explore possible reasons behind these slowly evolving anomalies in surface pressure from MY33 and MY34, other than changes in the total amount of atmospheric CO_2, one candidate process to consider is potential changes in the timing of the annual CO_2 cycle. Given the ability of HH to adapt to changes of frequency from exact subharmonics of a martian year, the absence of these slow trends in the pressure dataset minus HH fit suggests that interannual changes in the timing of maxima and minima could be contributing to the difference between harmonic fit and observations. Therefore an analysis was introduced to track the interannual changes in pressure maxima and minima and see their variability in relation to the long lived pressure biases.

Two steps were applied to estimate the timing of the maxima and minima in surface pressure from the available data and overcome the influence of data gaps after the MY34 GDS. In the first step a fit of the sol average surface pressure values, $\bar{p}_s$, near each pressure maximum and minimum was done to a sum of two sine functions of L_s whose amplitude, period, and phase were free fit parameters. This first fit delivered an estimate for the L_s when each extreme was reached and, in a second step, the fit was repeated but using only daily average surface pressures for L_s within a symmetric window of width $\sim$35° around the first estimate. The resulting refined L_s were taken as the times for the pressure maxima and minima. In a final iteration, the average L_s of all years p_{min} and p_{max} was taken as center of the time window for every minimum and maximum search before repeating the fit a third time. Changing the width of the temporal data window around the first guess from $\pm 20°$ to $\pm 50°$ in L_s maintained the refined L_s estimates to within 0.7°, depending on the particular peak. Thus the error bar in determining the L_s is taken to be 0.7°. This uncertainty level corresponds to less than 1 sol, since one sol corresponds to an increment of about $\sim 0.5°$ to 0.7° in L_s depending on the season. The L_s window eventually selected was $\pm 35°$ because it returned the smallest sum of standard deviations between fits and observations for all the periods around the minima and maxima, but that also implied that we could not fully calculate the late p_{min} for MY36 since the data record at the PDS did not yet cover all the required sols to perform this fit. Therefore MY36 shows question marks in Table 1.

Surface pressure maxima were reached every year over Mars Years 31-36 in Gale late Southern Hemisphere (SH) spring, shortly after perihelion, at $L_s \sim 255°$, and

MY	Pre-aphelion p_{max}	ΔL_s	Late NH Summer p_{min}	ΔL_s	Post-perihelion p_{max}	ΔL_s	Late SH Summer p_{min}	ΔL_s
MY31	N/A	N/A	N/A	N/A	254.15°	88.95° (146.2 s)	343.10°	74.70° (153.8 s)
MY32	57.80°	95.45° (202.0 s)	153.25°	101.15° (166.9 s)	254.40°	89.35° (147.0 s)	343.75°	74.30° (153.2 s)
MY33	58.05°	94.70° (200.5 s)	152.75°	101.30° (167.3 s)	254.05°	89.40° (147.0 s)	343.45°	71.70° (147.3 s)
MY34	55.15°	96.30° (204.4 s)	151.45°	103.55° (171.2 s)	255.00°	87.95° (144.6 s)	342.95°	74.65° (153.6 s)
MY35	57.60°	95.40° (201.9 s)	153.00°	102.70° (169.3 s)	255.70°	87.80° (144.5 s)	343.50°	73.30° (150.9 s)
MY36	56.80°	97.05° (205.3 s)	153.85°	102.30° (168.4 s)	256.15°	??	??	
Means±σ	57.47°± 0.60°	95.46° ±0.57° (202.2±1.4)	152.84° ± 0.61°	102.17° ±1.00° (168.7±1.7)	255.05° ±0.72	88.69° ±0.69°° (145.9±1)	344.08° ±0.39°	73.73° ±1.13° (151.8±2.5)
MY12$_{VL1}$			148.37^o	102.01^o	260.38^o			
MY12$_{VL2}$			149.12^o	100.07^o	259.82^o			
MY13$_{VL1}$			148.07^o	104.68^o	262.75^o			
	SP condensation rate seems faster than NP sublimation		SP reaches maximum	SP sublimates	Rate of NP condensation seems faster than SP sublimation		NP reaches maximum	NP sublimates

Table 1. Times of the maxima and minima in surface pressure measured by REMS in Gale and description of what transitions they mark in terms of the Northern Pole (NP) and Southern Pole (SP) caps behaviour. Red font marks the earliest and latest occurrences that are more than the larger of either one standard deviation σ or one sol $\sim$ 0.7°. Question marks are shown where there were not enough data to estimate the last minimum of MY36. Values are discretized in increments of 0.05°. Outliers occurred mostly in MY33 and MY34. ΔL_s measures the time increment between a p_{max} or p_{min} and the following p_{min} or p_{max} in degrees of areocentric longitude and in sols "s". The average time intervals beetween the p_{min} associated to the beginning and end of the SP growth season is 354.0±3.9 sols and 314.6±2.7 sols for the NP growth season.

in NH spring shortly before aphelion, at $L_s \sim 58°$. The local pressure minima are reached every year when the SP or the NP transition from a condensing (=expanding) to sublimating (=retreating) cap regime. Those moments are when the atmospheric column above Gale is at its lightest. They approach typically the maximum extent of each polar cap and occurred according to REMS pressure data in the late SH winter at $L_s \sim 153°$ and in late NP winter at $L_s \sim 344°$ before the NH spring equinox. The Viking Lander 1 and 2 estimates published for years MY12 and MY13 (Tillman et al., 1993) are included for comparison. They show a similar duration of the SP cap retreat phase, but an earlier start at $L_s \sim 149°$. Since both Viking landers were located north of Gale crater, this earlier p_{min} is suggestive of either interdecadal variability or a measure of the time difference that the global circulation requires to transfer the information about the CO_2 ice depletion rate in the NP from higher Northern latitudes to Gale. Similarly, a later maximum is visible at $L_s \sim 260°$ in VL vs. REMS.

Interannual changes in the timing of these maxima and minima at a given location on Mars are likely due or related to differences in the rates and lengths of the polar cap sublimation-condensation cycles. The largest deviation occurred for the pressure maximum near aphelion of MY34 when CO_2 peaked at $L_s = 55.15$, 1.65°-2.9° before all the other SH springs, up to nearly 3 degrees difference. Another anomaly is found in the length of the late MY34 NP Summer sublimation season, which after starting at L_s=342.95° was followed by the earliest NH Summer p_{min} accross all the years in MY34 GDS at $L_s \sim 151.45°$. These changes correspond to about 5 sols difference at most. Weather variability is likely to cause such deviations, e.g. what day does a dust storm or storm front come through, either dropping snow or accelerating/delaying slightly the defrosting due to atmospheric temperature changes.

After exiting the shortest NP sublimation season in MY32-MY33, the total duration between the pressure signatures limiting the MY33 SP growth cycle was the shortest on record at 351.7 sols against the four sols longer 355.8 sols expansion cycle of MY31. This is consistent with previous reports of an early storm in MY25 resulting in an acceleration of SP ice depletion (Piqueux et al., 2015), although MARCI data did not find signs of an unusual retreat or sublimation of the SP cap in MY34 (Acharya et al., 2023) –unlike in MY25. A possible explanation is that MCS measures CO_2 and MARCI maps the CO_2 and water ice caps.

The difference, $|\Delta|$, between fit and data decreased as MY34 started until the aphelion maximum surface pressure was reached on $L_s = 55.15°$, earlier than any other year. The positive pressure bias, shown in better detail in Figure 1(b) bottom panel, indicates that the atmosphere was heavier than other years by about 2.5 - 4.5 Pa ($\sim 0.4\%$) when the SP cap started expanding at a faster pace than the NP cap was retreating. For surface pressure to remain higher, the transition into the SP expansion regime had to occur after the NP cap would have released more mass than in previous years. This is consistent with a short SP cap growth and NP cap retreating season between $L_s = 343.45°$ and $L_s = 55.15°$ ($\Delta L_s = 55.15°_{MY34} - 343.45°_{MY33} =$ 71.7°=147.3 sols, against $\Delta L_s = 73.73°$ =151.8 sol averages) if the SP cap was not condensing as much mass as the NP was sublimating, or not fast enough. The change in duration suggests that there could be more CO_2 in the atmosphere between MY33 $L_s \sim 254.05°$ and MY34 $L_s \sim 55.15°$.

Some time later the GDS began, that seems to have reduced the positive pressure bias in Figure 1(b), and produced a lower surface pressure than expected from the fit. After the minimum pressure, p_{min}, was reached at an early $L_s = 151.45°$, the pressure curve returned to close to the seasonal value, matching a consistent timing of the event. The early $L_s = 151.45°$ start of SP cap sublimation seemed to increase the positive pressure bias again before reaching a maximum shortly before the storm changed the pressure bias in Figure 1(b) to negative. This also prolonged the SP cap sublimation season into the latest ($L_s = 255°$) occurrence out of the first four years with a duration of $\Delta L_s = 103.55°$ compared to the typical values of nearer to 102.17° from most years, or about 2.5 sols longer.

At the end of MY34 an early start to NP sublimation cap finished the second shortest period between p_{max} and p_{min} marking the NP cap growth season of the first 5 years, $\Delta L_s = 342.95° - 255.00° = 87.95°$. But having followed the earliest occurrence of a late NH Summer p_{min} at $L_s = 151.5°$ MY34 still resulted in the longest period of total NP cap expansion at 315.8 sols. Two sols more than the shortest period in MY35. Figure 1(b) shows a coincident surface pressure decrease with respect to the fit with the trend observed after sol 2040 in the blue line of the central panel on Figure 1(a). This was followed by a long period of SP cap growth in Table 1 into the pre-aphelion p_{max} of MY35, which happened at $L_s \sim 57.6°$.

The differences between MY33 and MY34 biases can be summarized by a MY33 bias that decayed slowly due to an earlier timing of the post-perihelion maximum, later SH Summer minimum, and by a pressure bias after the MY34 GDS that maintained ~3-6 Pa negative deviation from the zero line predicted by the fit in Figure 1(b) lower panel. The even earlier timing for the subsequent MY34 pressure minimum than in MY33 is likely attributable to a different process than the phase shifts in the timing of L_s that occurred during sols $\sim 1690 - 2040$.

At sublimation and condensation rates comparable to the other years, the delay in this transition would imply a heavier-than-normal atmosphere. The bottom panel in Figure 1(b) shows that the negative bias, Δ, started at $L_s \sim 198°$. This is during the very dusty phase of the GDS, but while REMS UV observations suggest peak opacity at $L_s = 195°$, the surface pressure observations and MCS dust and temperature retrievals indicate the peak of the storm occured at L_s=205^o-210^o (Viúdez-Moreiras et al., 2019), coincident with reaching the first minimum Δ in Figure 1(b). The bias then approaches zero again, nearly disappearing during the C storms season that followed the GDS, before moving back towards the original negative values as the C storms settled.

Analyses of Viking data provide hypotheses for the types of processes that may have happened during previous storms. Observations and model predictions for the effect of increased dust opacities at the Viking Landers locations (Hourdin et al., 1995) concluded that there was a delay in reaching the NH fall surface pressure maximum and that this maximum was lower than in years with low atmospheric opacity. The delay in surface pressure the peak following the MY34 GDS happened only slightly later, $L_s = 255$, about 1 sol after previous years in Gale crater. The rates of sublimation and condensation on the polar caps will be influenced differently by dust through changes in their emission and albedo caused by dust settling on the poles (Wood & Paige, 1992; Kahre & Haberle, 2010; Zhao et al., 2021). Additionally, depending on the dust vertical distribution, the atmosphere can get warmer or colder during a dust storm to increase sublimation over the SP, while an abundance of airborne aerosols reaching the NP can radiatively cool the atmosphere and provide ice condensation nuclei promoting ice deposition on the NP.

Another consideration is if the fitted scale heights, H, capture correctly the effect of altitude changes in our analysis of daily pressure averages (e.g. Lange et al., 2022, section 3.2). Figure 2 shows that the scale heights, while differing in value for the years shown in the different panels of Figure 1, correct for altitude changes independently of the time length used for the fit, in this case for the temporal window that covered four full years, by comparing the evolution of the pressure curves between the NP winter minimum $L_s \sim 155°$ until $L_s \sim 390°$, after the SH spring maximum. They are separated by year and multiplied by an exponential function of height and pressure scale height to correct for altitude effects. The curves overlap very well for all years until the L_s when the NP cap retreat starts, from which point the curves show differences between MY34 and the previous years. Daily average surface pressures are

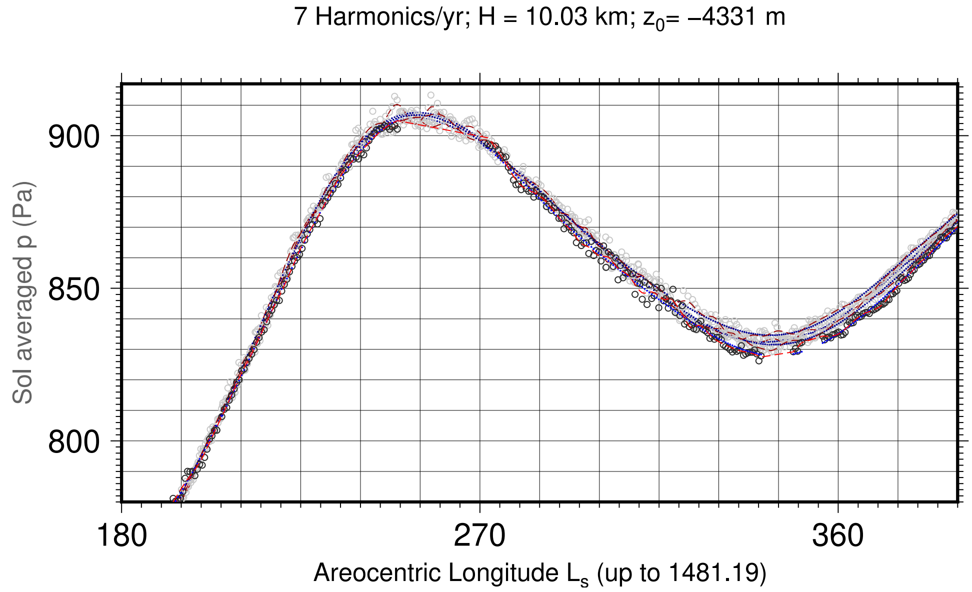

Figure 2. Observed surface pressure averages from the first 4 years on Gale and fits to the exponentially dependent series of harmonics from equation (2) separating year by year and shown after exponentially projecting to the same $z_0 = -4331\ m$ using the same scale height, $H = 10$, extracted from the fit to all years in Figure 1. To compensate for MY31 data being available only after $L_s = 155$ and MY35 reaching only into $L_s = 45°$, years are considered in this figure as intervals of 360° that span from $L_s = 30°$ to $L_s = 390°$ instead of using natural years from $L_s = 0°$ to $L_s = 360°$. The pressure averages to height z_o are $p_{s0} = 824, 834, 835, 835$ Pa for each period. The amplitudes of the first annual mode are $p_{s1} = 53, 54, 54, 50$ Pa, for the semiannual mode $p_{s2} = 58, 58, 56, 56$ Pa, and their phase shifts are $L_{s1} = 120.6°, 122.7°, 122.2°, 122.0°$ and $L_{s2} = 136.7°, 137.1°, 137.7°, 136.7°$ for each year. The last period is shown in dark grey open circles and the earlier the year the lighter the grey circles. The Hilbert Huang fits to guide the eye are shown in solid lines, darker red for the previous years and light red for the last year. Dark blue shows the fits to the series of harmonics projected into the z_0 height.

shown as light grey circles, and the MY34 into MY35 transition period is shown in dark grey. The numerical values for the annual and semiannual pressure modes in the fit to the observed annual pressure cycle do not show a significant difference either in the amplitudes or the phases of the pressure annual and semiannual modes. The annual fit for the first year has a larger uncertainty when extrapolated to a common height. This is attributed to the facts that it did not cover enough altitudes, and that data are not available until after the annual pressure minimum, thus causing a bias of the average pressure towards the lower values near the end of the martian year. The average pressure value of the fit to that first year dataset extrapolated to the altitude z_o at the center of the MSL traverse led therefore to a lower average pressure, $p_{s0} = 824$, Pa than in the other years. The other year's pressure amplitudes are more consistent with each other.

Focusing on the annual modes with higher frequencies for the pressure cycle, there are two changes consistent with the simulations from the Viking era: a significantly lower amplitude and phase of the annual mode. This mode is associated with changes in symmetry of the NH spring/fall pressure cycles and turned out to be (52.9 Pa, 52.6 Pa, 50.8 Pa, 52.7 Pa, 52.6 Pa) in Mars years 32 to 36 respectively after separating the fit for each year and correcting all of them with a scale height of 10735 m and a fit to 8 harmonics like in Hourdin et al. (1995). It thus made MY34 the lowest annual mode of the 6 years considered in the fit. For the pseudo-semiannual harmonic the situation reverses with an amplitude for the same years of (1.07, 1.06, 1.11, 1.08, 1.09) times that of each year's first mode. This shows a higher relevance of the semiannual variability in MY34.

The fact that the pressure deficit lasted longer than any known dynamical phenomenon, and that it happened only in MY34 and not the other years, should eliminate dynamical effects. Orographic and topographic effects are unlikely to act differently in MY34 than in the other years since the rover location has remained within 1 degree of latitude and longitude. One remaining option is that this pressure deficit is measuring a signature of a change in the extent of the NP ice cap. We describe next the MCS data analysis to test this hypothesis.

3 MCS Analysis of the NH polar cap evolution after the storm

At the surface of Mars, CO_2 ice temperature is buffered and only controlled by the local partial pressure. In other words, CO_2 ice is associated with diurnally invariant temperatures, a behavior unlike any other material including water ice. Leveraging this unique property, the presence of CO_2 ice can be mapped by comparing AM and PM surface temperatures, with CO_2 being the main gas in the atmosphere, it is present where no diurnal variations are found. With this approach, first described by Piqueux et al. (2015), no assumptions concerning ice emissivity (i.e., crystal size, or dust/water contamination) or local atmospheric pressure (i.e. CO_2 ice temperature) need to be formulated.

Here we reproduce their approach (Piqueux et al., 2015) to compare the MY34 seasonal cap during and after the 2018 GDS with that of other years during the MRO era and as presented in de la Torre Juárez et al. (2019). In short, we analyze data generated by MCS (McCleese et al., 2007), a nine band visible and thermal infrared radiometer designed to retrieve atmospheric and surface properties, including temperatures at ∼3AM/3PM local mean solar time. We only utilize retrieved (i.e., atmospherically corrected) surface observations at ∼32 μm because they provide the best estimate for surface brightness temperatures, the highest signal for cold targets, and benefit from a transparent atmospheric window. Surface temperature observations are binned at 1 pixel per degree spatial resolution and $15° L_s$. See the mapping uncertainty analysis in Piqueux et al. (2015). Although CO_2 ice is theoretically associated with ∼0K diurnal variations between 3AM and 3PM, we follow the recommendation by Piqueux et al. (2015) to set a 5K diurnal temperature threshold for CO_2 ice in order to account for instrumental, retrieval, or atmospheric noise and to account for the fact that the atmosphere is not fully transparent at 32μm (to be compared with ∼80+K diurnal variations for most surface materials). Finally, unlike the original cap mapping work of Piqueux et al. (2015) that relied on data acquired under very different conditions of surface emission angle (nadir vs. $\sim 70°$) by two different instruments (i.e., TES and MCS), we only use one homogenous dataset here (from MCS). This difference allows a direct comparison between the CO_2 cap sizes without performing emission phase function corrections. This procedural difference is inconsequential given the nature of the work presented here, i.e., a comparative study of cap sizes within the MCS dataset, but explains some differences in absolute surface area values to those given in (Piqueux et al., 2015). Cap mapping during and after the 2018 GDS using MCS data shows no uniqueness in the South compared to other MY. For comparison, the MY 27 GDS occurring at a similar season showed a clear impact on the (accelerated) retreat of the cap that year (Piqueux et al., 2015). In the North, the retreating MY34 seasonal cap following the 2018 GDS is the largest of the MRO era (Figure 3), suggesting a delayed waning, in contrast with the accelerated cap retreat in MY 28/29 following the GDS observed that year (Piqueux et al., 2015). At the peak of the difference, near $L_s \sim 322°$ the difference in cap surface area between MY34 and the MY28-34 average is ∼3-4 x 10^5 km^2, or $< 1°$ in equivalent latitude, a subtle difference, comparable to the method's resolution, but locally larger as is visible in Figure 3(b). The full polar cap is shown in the supporting information Figure S1. The differences appear similar at all longitudes.

Given that the SP cap did not show any deviations after the MY34 GDS with respect to previous years, one would expect the atmosphere to have a similar amount of CO_2 and water vapor from the SP sublimation as in the previous year. However, a lower atmospheric mass is required to explain the REMS observation of a lower surface pressure in Gale crater after the dust storm. Another location where that mass could be stored is the NP cap. The ensuing increase in NP surface cap area would be consistent with a decreased amount of atmospheric CO_2. If this is the mechanism, the pressure anomaly should last as long as the NP cap. Once the cap would start retreating and sublimating ice into the atmosphere, the surface pressure level could return to typical levels, and this is what appears in the right panel of Figure 1.

4 MCS observations of zonally averaged temperature anomalies

After finding a larger NP cap extent, there is value in providing modelers with MCS observations that might help clarify which of the several processes identified since the Viking era (e.g. Hourdin et al., 1995; Wood & Paige, 1992; Kahre & Haberle, 2010; Zhao et al., 2021) have the potential to connect the MY34 dust storm with the larger extent of the NP cap that followed. MCS observations of zonal mean temperatures, ice clouds, and CO_2 clouds either constrain the models or support some of the potential processes. MCS profiles of temperature, dust and water ice as well as surface temperature, dust and water ice column amounts (Kleinböhl et al., 2009, 2011, 2017) are retrieved from MCS limb radiance profiles. These are standard v5.2.4 profiles as delivered to PDS. We compare MY 34 to other MY measured by MCS, with a focus on MY 33. Noting that MCS sensitivity is probably ~ 1 K in zonal mean average, differences were observed between 1 to 3 K which are marginally above the MCS noise floor in the winter polar vortices. In MY34 polar temperatures were marginally cooler, primarily a "daytime" effect (near 3 pm LTST). Nighttime data showed also very slight temperature effects of the sampling bias, primarily centered around ∼25 km.

What is the potential actual effect on the surface, especially on the seasonal CO_2 cap? MCS observed a water ice polar hood that was thinner at altitude, but thicker

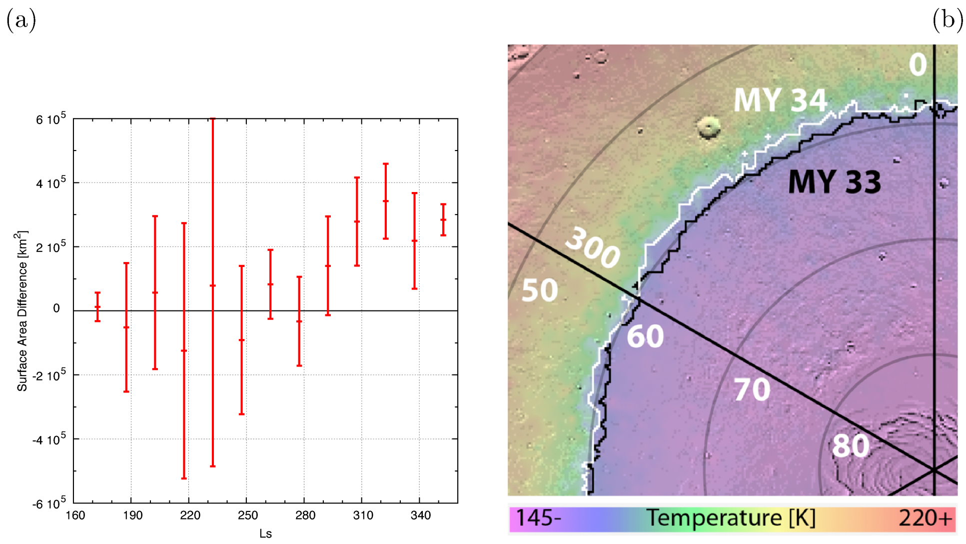

Figure 3. Difference between the North seasonal cap surface area in MY34 versus the median of the MRO era (MY28-34), see text for mapping procedure. During its retreat (past L_s 270), the MY34 seasonal cap is the largest of the MCS-MRO era and noticeably larger than the median. Positive values indicate larger caps compared to the median; (b) Comparison between the MY34 (white) and MY33 (black) North caps (315< L_s <330). The MY34 cap appears slightly larger than the MY33 cap at this season. Background is 3PM MCS surface temperature (MY34) and MOLA shaded relief. The image is magnified, showing only one quarter of the cap, to better see the differences. Latitude gridding every 10° from 80° to 50°, Longitude every 60° (300° and 0°).

near the surface. The changes are fairly modest in both cases, maybe 25%. The reduction of clouds that appears with the lower temperature helps discern between two competing hypothetical mechanisms. Lower temperatures at 50 Pa normally result in increased clouds which would have a greenhouse effect and increase temperatures below the clouds. However, near the surface, lower temperatures also decrease the relative humidity and promote condensation and ice deposition on the planet surface. MCS found CO_2 snow clouds to be preferentially forming at the NP and at low altitudes near 500 Pa, compared to MY33, with a lack of clouds away from the Pole in the vortex. The differences between MY33 and MY34 remaining mostly $< 25\%$ in both regions.

The panels in Figure 4 show different diagnostics of the circulation after the decay of the Dust Storm. Its top left and center panels show the temporal evolution of zonal mean daytime and nighttime temperatures at 50 Pa as a function of latitude and areocentric longitude. These differences in MY34 after the GDS against a median of all MY covered by MCS data at this season – MY 28 to 34– and during the sublimation of the SP cap, show a dominant warm feature seen in the differences in Figures 4(a) and 4(b). It is the MY 34 post-solstice large-scale regional C dust event (Kass et al., 2016) which was seasonally late and strong. Likewise, the very cold feature before it is an echo of the more standard C event seasonal timing. The warm feature at high southern latitudes from L_s 280° to 285° is the end of the polar B large scale regional dust event which was somewhat warmer than usual (with a sharper than usual end). The warmer SP than previous years would have enhanced sublimation of the SP cap. At the same time, the same panel shows that while most latitudes shared a warm bias, there was a colder NP atmosphere because of the late C storms and a dustier atmosphere than typical for this time of the year, what would have favored ice condensation. A colder atmosphere that favors ice formation would lead to clouds unless the ice deposits on the surface. The rightmost panel on the top shows a lower amount of total atmospheric ice column in MY34 than in median MY33 at all latitudes. This would be consistent with the water ice being deposited on the surface.

The bottom panels in Figure 4 show how the different altitudes may have contributed to those differences between MY33 and MY34. The bottom left panel shows that the cold MY34 zonal temperature differences are focused from 50 Pa down to ~200 Pa, or approximately the second scale height above the surface. The higher temperatures in the south do not extend to the surface and thus do not affect the retreat of the southern polar cap. The effect of these low altitude biases after the GDS is consistent with a SP retreating after the GDS at a similar rate than in MY33, but an NP expanding at a faster rate. The central bottom panel in Figure 4 shows the differences in MY34-MY33 dust for this season for most latitudes. However, due to a limitation of the MCS retrieval algorithm within the northern polar (winter) vortex, it is the signature of CO_2 clouds poleward of 65 N (Hayne et al., 2012). At most latitudes, the atmosphere below ~20 Pa is moderately dustier in MY34 (consistent with the slightly higher temperatures). This includes above the SP where increased dust might affect the sublimation of the SP cap. Above the NP, there is a deficit of CO_2 clouds compared to MY33 except right at the pole. This could indicate an increase of CO_2 near the pole from CO_2 snow, but more importantly due to energy balance, it may instead allow for increased surface CO_2 frost deposition by allowing for easier radiation to space and thus increased surface cooling. The increased snow at the north pole may also delay its sublimation due to the necessity for a higher (seasonally later) sun. Given that this occurs during a colder NP regime, one possible mechanism is that the NP has been receiving higher amounts of CO_2 deposits than in MY33. The larger extent of the NP cap described in Figure 3 supports this potential mechanism. It is interesting however to contrast this observation with the right column of Figure 4 showing the amount of water ice as a function of height in the rightmost bottom panel. It suggests that, while there were few clouds at high altitudes, the lowest scale height

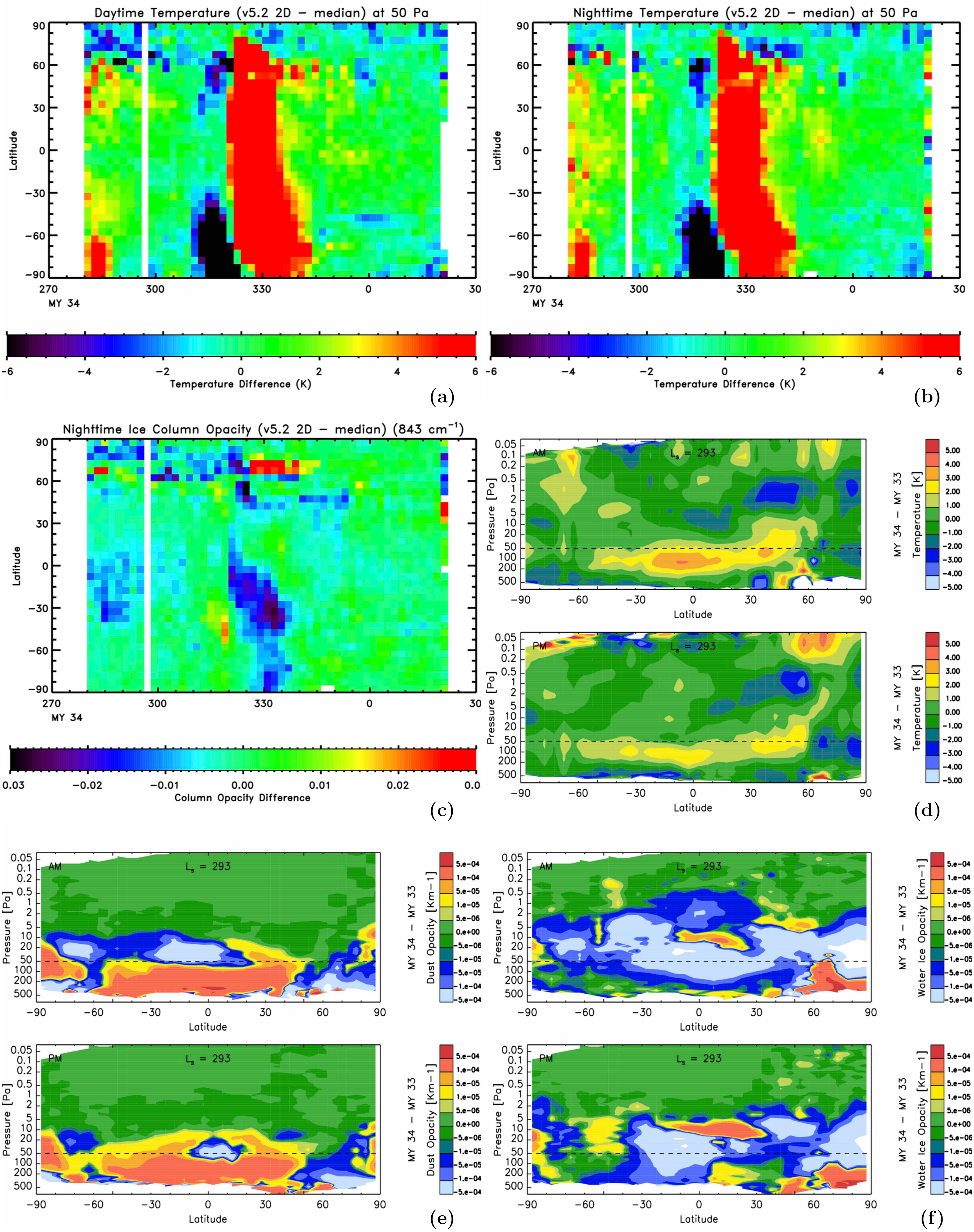

Figure 4. (a) Zonal mean daytime temperature deviations at 50 Pa as a function of L_s after the GDS; (b) Zonal mean nighttime temperature deviations after the GDS; (c) Zonal mean nighttime ice column during these temperature maps. MY34-MY33 zonal mean differences averaged over the period $L_s = 281°$ to $L_s = 305°$ in the AM MCS pass (top sub-panels) and PM (lower sub-panels) for: (d) temperature; (e) dust, except north of 65 N where it is CO_2 ice clouds, and (f) Water ice clouds.

displayed an overabundance of ice clouds. At the same time, the total column opacity was slightly less, at least in AM times, which would have favored more efficient net radiation transfer to space from the surface.

5 Summary and Conclusions

An analysis technique is presented here of the timeline of martian surface pressure changes, as Curiosity has been roving up from the bottom of Gale crater, to infer first the vertical scale height of a best fit hydrostatic model of the atmospheric layer inside Gale. This fit to equation (2) models the effect of the changing rover altitude, sensor trends, and seasonal effects. That fit is then compared with the observed sol averages of surface pressure, and the differences are explored over the period covering MY31-MY36. Two years stand out as anomalies in the timing to reach the pressure maxima and minima, and both anomalies fall on either side of the MY34 GDS. The analysis focuses on the main differences in timing that occurred in Mars year 33 and 34. These differences might be responsible for slowly varying pressure offsets compared to the rest of the years. The small MY33 offsets predate and are not attributable to the MY34 Global Dust Storm. MY33 started with an apparent sudden offset towards a higher surface pressure followed by a slow trend towards seasonal values followed by another increase in atmospheric pressure, compared to the seasonal values from a five-year climatology. The latter offset started slowly and then reversed shortly before the GDS, ultimately overshooting to give a deficit in surface pressure compared to previous years. After reaching its highest opacity, the MY34 dust storm atmosphere transitioned to a lower surface pressure by 0.3-0.4%. While the analysis shows that a potential MY33 bias was accompanied by shifts in the length of the polar caps expansion-retreat cycles, in MY34 the pressure deficit lasted for more than 100° L_s. The long duration and the timing of the MY34 anomaly is only consistent with the time scales and duration of the NP ice cap growth cycle. This suggests that Gale recorded a pressure signature of a deficit of atmospheric CO_2 and is coincident with an above average NH polar cap surface extent. Both results, a lighter atmospheric column over Gale crater and a larger polar ice surface at the North Pole, suggest a higher volume of ice at the cap as well.

Recent works with other sensors (Alsaeed & Hayne, 2022; Acharya et al., 2023) have confirmed the MCS observation of a larger NP ice cap. InSight data (Lange et al., 2022) were combined with MSL and atmospheric Global Circulation Model output to also suggest a larger NP extent after the early MY34 GDS. The novelties of the present work are its purely observational approach, an analysis of MCS observations of polar hood temperatures, and the multiannual comparison of pressure cycles that enable the identification of changes in the duration of the Polar cap expansion-contraction cycles around the years before and after the storm. These changes might hopefully provide clues about what other processes, only captured by modeling studies, are consistent with the Gale observations.

We are also addressing here the question whether the pressure deficit in REMS data could be a signature of other phenomena that could affect Gale. Panels in Figure 1 have shown that the duration of the pressure deficit outlasts any other dynamical effects. After quantifying the effect of pressure sensor drifts, an analysis was done on the effects of shifts in the timing of the pressure minima and maxima in response to the variability of the growth and depletion cycles of the polar ice caps. Continuing with dust effects, the deficit reported lasted well beyond the dust season, including a C storm season of large amplitudes that followed the GDS. Baroclinic waves, often associated with weather systems, last only for a few sols and are visible in Figure 1. They add to the variability but do not eliminate the pressure deficit. Hourdin et al. (1993) and Hourdin et al. (1995, including proper feedbacks) used a primitive equation model to identify the influence of multiple effects on surface pressures and the authors described geostrophic adjustment and orographic effects as important sources of pressure anomalies at least at high latitudes. Gale is at an equatorial latitude of 4.5° S. Proper quantification of geostrophic effects at the equator needs a model that includes the horizontal component of the Coriolis force (e.g. de Verdière & Schopp, 1994; White & Bromley, 1995; de la Torre Juárez et al., 2002). This term is absent in primitive equation models, which use the shallow layer hydrostatic approximation. If the GDS caused any geostrophic adjustment in pressures at equatorial latitudes, it is unclear why they would continue much longer than the storm itself. Other dynamical features that would evolve on such long scales are perturbations to the Hadley cell, caused by changes to angular momentum redistribution by the GDS. These cannot be excluded, but the question remains for why would they survive the GDS. Changes in the polar cap cycle might, however, induce changes in the Hadley cell circulation on the time scale of the polar cap cycles and therewith explain the surface pressure anomalies, but this would mean that the ultimate mechanism creating the pressure deficit is the anomaly in the NP ice cap cycle.

Other phenomena that might cause shifts in surface pressure are the potential role of Gale topography on the internal crater circulations. The effects of crater topography have been shown to amplify the amplitude of the diurnal pressure tides on Gale due to hydrostatic adjustment flows (Tyler & Barnes, 2013; Richardson & Newman, 2018) in response to daily thermal forcing, on diurnal time-scales. These effects on diurnal and sub-diurnal tides are absent in an analysis of daily averages. Another possible effect from (e.g. Hourdin et al., 1993) is the planetary-scale orographic effect that emerges when comparing surface pressures from locations separated by many degrees in latitude. Since Curiosity has not abandoned Gale, the exposure to effects of changes in topography and orography should be mostly captured by changes in altitude, as latitude or longitude have remained constant to within one degree. As Curiosity kept climbing, MY36 returned to a behavior more similar to all years before the GDS of MY34 than to MY35, thus underscoring the uniqueness of the season after the GDS.

Finally, a concern remained about selecting a fixed H and ignoring the diurnal and seasonal changes in temperature. H is not prescribed here but inferred from the data themselves, while those concerns are important when using data to interpret the value of H and connect it to a Global Circulation Model (GCM), the use of different time windows to calculate H has been shown in this observational technique to repeatedly find the pressure deficit for multiple time windows and values of H. The resilience of this pressure deficit to multiple attempts to eliminate it provides a cross-validation of the conclusions based on model simulations by Lange et al. (2022).

In MY33 and early MY34, the pressure maxima and minima occurred at different times compared to other years. This led to deviations in the length of the NP and SP ice cap retreat and growth seasons (before the storm) with the shortest NP cap retreat period of all years recorded by about 4 sols in MY33-MY34 by REMS at $\Delta L_s \sim 71.7° + 96.3°$ followed by the longest SP retreat at $103.6° + 87.9°$ but at a potentially smaller rate, since the SP did not show a deviation in the rate of surface ice retreat. It is worth exploring if the anomalies before the dust storm may have influenced the GDS occurrence but were not associated with any detectable anomalies in the size of the polar caps. However, the anomaly observed in MY34 after the dust storm that followed the four sols early stop of SP growth, is a longer NP growth season by about 2 sols, and did coincide with a larger extension of the NP cap. Previous early Global dust storms have been followed by larger NH polar caps, as observed by orbiters in 1977 and in MY25 (Zurek, 1982; Piqueux et al., 2015). This has been attributed to an expansion of the Hadley cell or an increased northward Eliassen-Palm flux into the higher altitudes caused by stationary waves (Bougher et al., 2006; Kuroda et al., 2009). In both cases an increased transport of CO_2 and water vapor from SP to NP would be the predicted result and is consistent with recent observations (Fedorova et al., 2020).

Table 2. Timing of key observations.

MY	Surface Pressure observation	Related MCS observation	Effect
31	Poor fit to height dependent pressure because of an insufficient time record. Average timing for pressure minima and maxima, i.e. start of polar caps expansions and retreats	N/A	N/A
32	Average timing for pressure maxima and minima	Average Polar cap surface extents	
33	Early start of SP cap condensation rate overtaking the rate of NP cap depletion	Used as reference to compare to MY34 global circulation properties	
34	GDS storm starts on $L_s \sim 190°$. Starts decaying at 195° Before GDS: Earliest start of NP retreat among MY31-MY34. Early start led to a high pressure bias The NP cap expansion finishes the shortest of all the three years, at $\Delta L_s \sim 71.7°$followed by the longest period of SP retreat and NP growth of MY31-MY34. Early start of SP retreat. High pressure bias associated with the early start of NP and SP retreats During GDS: high surface pressure bias transitions to deficit at the beginning of the Dust storm decay phase Longest period of SP retreat in MY34 into $Ls = 342.95°$. Low pressure bias nearly disappears in $L_s \sim 245° - 280°$ After GDS: pressure deficit returns near $L_s \sim 280°$ and increases. It starts decreasing after the NP cap starts retreating.	Typical size and recession rate of SP cap Largest NP cap surface from MCS NP cap reached the maximum extension from MY28-MY34	Change in time of pressure maxima and minima have a potential relation to the cause of the GDS Warm anomaly over southern latitudes at the end of GDS decay, near $L_s \sim 280°$. A $\sim$3 Pa surface pressure change corresponds to a $\sim$20 cm solid CO_2 ice layer over the area of difference in cap size between MY34 and MY33.
Other	REMS instrument drift likely less than ~ 0.5 Pa/yr		Effect removed in the fits, and smaller than the 3-6 Pa offset observed. Some impact in the apparent value of Scale height.

These hypotheses cannot be addressed with observations only, but the observations in this work may hopefully provide clues to test hypotheses from modeling studies.

Table 2 combines the MCS observations discussed in the previous sections and summarizes several mechanisms that might be consistent with the observations from REMS and MCS. They are (1) Increased radiation to space due to reduced clouds after the storm, which would slow sublimation from the SP; (2) Less snow addition to the cap would have resulted in higher emissivity and therefore enhanced radiative cooling; (3) more mass addition at the NP during SP recession.

6 Open Research & Data statement

All Mars Science Laboratory data necessary to reproduce each figure shown in this manuscript are available via the Planetary Data System (PDS) Atmospheres node (Gómez-Elvira & the REMS team, 2013). The REMS data used for this research were calibrated files for all the analyses following Gómez-Elvira et al. (2012). All the analyses were performed using python3 scripts and the Generic Mapping Tools software (Wessel et al., 2019). The pressure data, their fits and the filters are in (de la Torre Juárez et al., 2023). For the description of the approach and climatological cap edges, see Piqueux et al. (2015) and associated files; for the latest data used to generate updates, see McCleese and Schofield (2006), which is the DOI for the MCS data record. The associated description is McCleese et al. (2007)

References

Acharya, P. J., Smith, I. B., & Calvin, W. M. (2023). Tracking the northern seasonal cap retreat of mars using computer vision. *Icarus*, *390*, 115295. Retrieved from `https://www.sciencedirect.com/science/article/pii/S0019103522003876` doi: https://doi.org/10.1016/j.icarus.2022.115295

Alsaeed, N. R., & Hayne, P. O. (2022). Transport of Water Into the Polar Regions of Mars Through Scavenging by CO_2 Snowfall. *Journal of Geophysical Research (Planets)*, *127*(11), e2022JE007386. doi: 10.1029/2022JE007386

Barnes, J. R. (1981). Midlatitude disturbances in the Martian atmosphere: a second Mars year. *Journal of Atmospheric Sciences*, *38*, 225-234. doi: 10.1175/1520-0469(1981)038⟨0225:MDITMA⟩2.0.CO;2

Bell, J. F., Godber, A., McNair, S., Caplinger, M. A., Maki, J. N., Lemmon, M. T., ... Deen, R. G. (2017). The Mars Science Laboratory Curiosity rover Mastcam instruments: Preflight and in-flight calibration, validation, and data archiving. *Earth and Space Science*, *4*(7), 396-452. doi: 10.1002/2016EA000219

Bougher, S. W., Bell, J. M., Murphy, J. R., Lopez-Valverde, M. A., & Withers, P. G. (2006). Polar warming in the mars thermosphere: Seasonal variations owing to changing insolation and dust distributions. *Geophysical Research Letters*, *33*(2). Retrieved from `https://agupubs.onlinelibrary.wiley.com/doi/abs/10.1029/2005GL024059` doi: 10.1029/2005GL024059

de la Torre Juárez, M., Fisher, B. M., & Orton, G. S. (2002). Large Scale Geostrophic Winds with a Full Representation of the Coriolis Force: Application to IR Observations of the Upper Jovian Troposphere. *Geophysical and Astrophysical Fluid Dynamics*, *96*(2), 87-114. doi: 10.1080/03091920290027943

de la Torre Juárez, M., Piqueux, S., Kass, D. M., Newman, C., & Guzewich, S. D. (2019). Pressure Deficit in Gale Crater and a Larger Northern Polar Cap after the Mars Year 34 Global Dust Storm. In *AGU Fall Meeting Abstracts* (Vol. 2019, p. P51C-02). Retrieved from `https://essopenarchive.org/doi/full/10.22541/essoar.169945479.90436599/v1`

de la Torre Juárez, M., Piqueux, S., Kass, D. M., Newman, C. E., & Guzewich,

S. D. (2023). *Replication Data set for the article 'Pressure deficit in Gale Crater and a larger Northern polar cap after the MY34 Global Dust Storm.'* [Dataset]. JPL Open Repository. Retrieved from https://doi.org/10.48577/jpl.UHNK4U doi: 10.48577/jpl.UHNK4U

de Verdière, A. C., & Schopp, R. (1994). Flows in a rotating spherical shell: the equatorial case. *Journal of Fluid Mechanics*, *276*, 233-260.

Fedorova, A., Montmessin, F., Korablev, O., Luginin, M., Trokhimovskiy, A., Belyaev, D., … Wilson, C. (2020). Stormy water on mars: The distribution and saturation of atmospheric water during the dusty season. *Science*, *367*, eaay9522. doi: 10.1126/science.aay9522

Gómez-Elvira, F., & the REMS team. (2013). *Mars rover environmental monitoring station (REMS) experiment data record (EDR) and reduced data record (RDR) data products archive bundle.* [Dataset]. NASA Planetary Data System. Retrieved from https://pds.nasa.gov/ds-view/pds/viewDataset.jsp?dsid=MSL-M-REMS-4-ENVRDR-V1.0 doi: 10.17189/1523028

Gómez-Elvira, F. J., Armiens, C., Castañer, L., Domínguez, M., Genzer, M., Gómez, F., … Martín-Torres, J. (2012). REMS: The environmental sensor suite for the mars science laboratory rover. *Space Sci. Rev.*, *170*(doi 10.1007/s11214-012-9921-1), 583–640.

Guzewich, S., Lemmon, M., Smith, C., Martinez, G. M., Vicente-Retortillo, A., Newman, C., … Zorzano, M.-P. (2018). Mars science laboratory observations of the 2018/mars year 34 global dust storm. *Geophysical Research Letters*, *46*. doi: 10.1029/2018GL080839

Haberle, R. M., Juárez, M., Kahre, M. A., Kass, D. M., Barnes, J. R., Hollingsworth, J. L., … Kahanpää, H. (2018, June). Detection of Northern Hemisphere transient eddies at Gale Crater Mars. *Icarus*, 150-160. doi: 10.1016/j.icarus.2018.02.013

Harri, A. M., Genzer, M., Kemppinen, O., Kahanpää, H., Gomez-Elvira, J., Rodriguez-Manfredi, J. A., … REMS/MSL Science Team (2014). Pressure observations by the Curiosity rover: Initial results. *Journal of Geophysical Research (Planets)*, *119*(1), 82-92. doi: 10.1002/2013JE004423

Hayne, P. O., Paige, D. A., Schofield, J. T., Kass, D. M., Kleinböhl, A., Heavens, N. G., & McCleese, D. J. (2012). Carbon dioxide snow clouds on mars: South polar winter observations by the mars climate sounder. *J. Geophys. Res.*, *117*(E08014), 10.1029/2011JE004040.

Hourdin, F., Forget, F., & Talagrand, O. (1995). The sensitivity of the Martian surface pressure and atmospheric mass budget to various parameters: A comparison between numerical simulations and Viking observations. *J. Geophys. Res.*, *100*(E3), 5,501-5,523.

Hourdin, F., Le van, P., Forget, F., & Talagrand, O. (1993). Meteorological Variability and the Annual Surface Pressure Cycle on Mars. *Journal of the Atmospheric Sciences*, *50*(21), 3625-3640. doi: 10.1175/1520-0469(1993)050⟨3625:MVATAS⟩2.0.CO;2

Huang, N., & Wu, Z. (2008). A review on Hilbert-Huang transform: Method and its applications to geophysical studies. *Rev. Geophys.*, *46*(RG2006), doi:10.1029/2007RG000228.

Kahre, M., & Haberle, R. (2010). Mars CO2 cycle: Effects of airborne dust and polar cap ice emissivity. *Icarus*, *207*, 648–653. doi: doi:10.1016/j.icarus.2009.12.016

Kass, D. M., Kleinboehl, A., McCleese, D. J., Schofield, J. T., & Smith, M. D. (2016). Interannual similarity in the martian atmosphere during the dust storm season. *Geophys. Res. Lett.*, *43*, 6,111-6,118, 10.1002/2016GL068978.

Kleinböhl, A., Friedson, A. J., & Schofield, J. T. (2017). Two-dimensional radiative transfer for the retrieval of limb emission measurements in the martian atmosphere. *JQSRT*, *187*, 511–522.

Kleinböhl, A., Schofield, J., Kass, D., Abdou, W., Backus, C., Sen, B., ... Mccleese, D. (2009). Mars climate sounder limb profile retrieval of atmospheric temperature, pressure, and dust and water ice opacity. *J. Geophys. Res. (Planets)*, *114*. doi: 10.1029/2009JE003358

Kleinböhl, A., Schofield, J. T., Abdou, W. A., Irwin, P. J., & de Kok, R. (2011). A single-scattering approximation for infrared radiative transfer in limb geometry in the martian atmosphere. *J. Quant. Spectr. & Rad. Trans.*, *112*, 1568-1580.

Kuroda, T., Medvedev, A., Hartogh, P., & Takahashi, M. (2009). On forcing the winter polar warmings in the martian middle atmosphere during dust storms. *Journal of the Meteorological Society of Japan*, *87*, 913-921. doi: 10.2151/jmsj.87.913

Lange, L., Forget, F., Banfield, D., Wolff, M., Spiga, A., Millour, E., ... Banerdt, W. B. (2022). InSight Pressure Data Recalibration, and Its Application to the Study of Long-Term Pressure Changes on Mars. *Journal of Geophysical Research (Planets)*, *127*(5), e07190. doi: 10.1029/2022JE007190

McCleese, D. J., & Schofield, J. T. (2006). *MRO MARS CLIMATE SOUNDER LEVEL 4 RDR V1.0, NASA Planetary Data System, MRO-M-MCS-4-RDR-V1.0, 2006.* [Dataset]. NASA Planetary Data System. Retrieved from `{https://pds.nasa.gov/ds-view/pds/viewDataset.jsp?dsid=MRO-M-MCS-4-RDR-V1.0}` doi: 10.17189/4w08-hh34

McCleese, D. J., Schofield, J. T., Taylor, F. W., Calcutt, S. B., Foote, M. C., Kass, D. M., ... Zurek, R. W. (2007). Mars climate sounder: An investigation of thermal and water vapor structure, dust and condensate distributions in the atmosphere, and energy balance of the polar regions. *J. of Geophys. Res.*, *112*((E5)), doi:10.1029/2006je002790.

Medvedev, A. S., Kuroda, T., & Hartogh, P. (2011). Influence of dust on the dynamics of the martian atmosphere above the first scale height. *Aeolian Res.*, *3*, 145–156, doi:10.1016/j.aeolia.2011.05.001.

Newman, C. E., Lewis, S. R., Read, P. L., & Forget, F. (2002). Modeling the martian dust cycle: 2. multiannual radiatively active dust transport simulations. *J. Geophys. Res.*, *107*((E12)), 10.1029/2002JE001920.

Pascal, B. (1648). Oeuvres complètes. périer to pascal, 22 september 1648. (Paris: Seuil, 1960), 2:682.

Piqueux, S., Kleinböhl, A., Hayne, P., Kass, D., Schofield, J., & McCleese, D. (2015). Variability of the martian seasonal co2 cap extent over eight mars years. *Icarus*, *251*(164–180). doi: 10.1016/j.icarus.2014.10.045

Richardson, M. I., & Newman, C. E. (2018). On the relationship between surface pressure, terrain elevation, and air temperature. Part I: The large diurnal surface pressure range at Gale Crater, Mars and its origin due to lateral hydrostatic adjustment. *Planetary Sciences*, *164*, 132-157. doi: 10.1016/j.pss.2018.07.003

Ryan, J., & Henry, R. (1979). Mars atmospheric phenomena during major dust storms, as measured at surface. *J. Geophys. Res.*, *84*, 2821–2829.

Tillman, J. E. (1988). Mars global atmospheric oscillations: Annually synchronized transient normal-mode oscillations and the triggering of global dust storms. *J. Geophys. Res.*, *93*(D8), 9,433–9,451.

Tillman, J. E., Johnson, N., Guttorp, P., & Percival, D. B. (1993). The martian annual atmospheric pressure cycle: Years without great dust storms. *J. Geophys. Res.*, *98*((E6)), 10,963-10,971.

Tyler, J., D., & Barnes, J. R. (2013). Mesoscale Modeling of the Circulation in the Gale Crater Region: An Investigation into the Complex Forcing of Convective Boundary Layer Depths. *International Journal of Mars Science and Exploration*, *8*, 58-77. doi: 10.1555/mars.2013.0003

Viúdez-Moreiras, D., Newman, C. E., de la Torre, M., Martínez, G. M., Guzewich, S. D., Lemmon, M. T., ... Gómez-Elvira, J. (2019). Effects of the MY34/2018

Global Dust Storm as Measured by MSL REMS in Gale Crater. *Journal of Geophysical Research: Planets*, *124*. doi: 10.1029/2019JE005985

Wang, H., & Richardson, M. I. (2015). The origin, evolution, and trajectory of large dust storms on Mars during Mars years 24-30 (1999-2011). *Icarus*, *251*, 112-127.

Wessel, P., Luis, J. F., Uieda, L., Scharroo, R., Wobbe, F., Smith, W. H. F., & Tian, D. (2019). The Generic Mapping Tools Version 6 [Software]. *Geochemistry, Geophysics, Geosystems*, *20*(11), 5556-5564. Retrieved from `https://www.generic-mapping-tools.org/download/` doi: 10.1029/2019GC008515.

White, A. A., & Bromley, R. A. (1995). Dynamically consistent, quasi-hydrostatic equations for global models with a complete representation of the Coriolis force. *Quarterly Journal of the Royal Meteorological Society*, *121*(522), 399-418. doi: 10.1002/qj.49712152208

Withers, P. (2012). Empirical Estimates of Martian Surface Pressure in Support of the Landing of Mars Science Laboratory. *Space Science Review*, *170*(1-4), 837-860. doi: 10.1007/s11214-012-9876-2

Wood, S. E., & Paige, D. A. (1992). Modeling the martian seasonal co2 cycle: Fitting the viking lander pressure curves. *Icarus*, *99*, 1–14.

Zhao, Y., Zhong, L., Yuan, R., Zhao, C., Li, R., Wang, Y., … Richardson, M. (2021). Simulation of Martian Dust Effects on Polar CO_2 Ice Caps and Atmospheric Circulation Using the MarsWRF Model. *Journal of Geophysical Research (Planets)*, *126*(12), e06937. doi: 10.1029/2021JE006937

Zurek, R. (1982). Martian great dust storms: An update. *Icarus*, *50*, 288-310.

Zurek, R. W., & Martin, L. J. (1993). Interannual variability of planet-encircling dust storms on mars. *Journal of Geophysical Research (Planets)*, *98*((E2)), 10.1029/92JE02936.

Zurek, R. W., & Smrekar, S. E. (2007). An overview of the Mars Reconnaissance Orbiter (MRO) science mission. *J. Geophys. Res.*, *112*(E05S01), doi:10.1029/2006JE002701.

Zurita-Zurita, S., de la Torre Juárez, M., Newman, C. E., Viúdez-Moreiras, D., Kahanpää, H. T., Harri, A. M., … Rodríguez-Manfredi, J. A. (2022). Mars Surface Pressure Oscillations as Precursors of Large Dust Storms Reaching Gale. *Journal of Geophysical Research (Planets)*, *127*(8), e07005. doi: 10.1029/2021JE007005

Acknowledgments

We want to thank the patience and suggestions from the reviewers and the Associate Editor, Anni Määttänen, in helping make this manuscript more readable. This work was carried out at the Jet Propulsion Laboratory/California Institute of Technology under a NASA-MSL grant. MSL and REMS data are available at the Data Planetary System by courtesy the NASA and the Jet Propulsion Laboratory. U.S. Government support acknowledged. MTJ is indebted to Henry Kahanpää for noting the need to consider the role of year-to-year drifts in the pressure sensor. REMS and MCAM opacity data for sols up to 2358 are available at NASA's Planetary Data System (PDS) at https://pds.nasa.gov. Data for MCS at the PDS cover until $L_s = 333$ of MY34. Some REMS and MCS data after these dates have been included that do not change the conclusions and add strength to them as well as providing the most complete picture of the phenomena observed within the time frame of the publication. They include observations that remain prioritary to MCS and REMS until full validation of all other Curiosity and MRO instrument data has been completed.